

# Modeling and analysis of a 2-DOF bidirectional electro-thermal microactuator

Caglar Elbuken · Nezih Topaloglu ·  
Patricia M. Nieva · Mustafa Yavuz ·  
Jan P. Huissoon

Received: 28 August 2008 / Accepted: 16 January 2009  
© Springer-Verlag 2009

**Abstract** In this paper, a four hot-arm U-shape electro-thermal actuator that can achieve bidirectional motion in two axes is introduced. By selectively applying voltage to different pairs of its four arms, the device can provide actuation in four directions starting from its rest position. It is shown that independent in-plane and out-of-plane motions can be obtained by tailoring the geometrical parameters of the system. The lumped model of the microactuator was developed using electro-thermal and thermo-mechanical analyses and validated using finite element simulations. The device has been fabricated using PolyMUMPs and experimental results are in good agreement with the theoretical predictions. Total in-plane deflections of 4.8  $\mu\text{m}$  (2.4  $\mu\text{m}$  in either direction) and upward out-of-plane deflections of 8.2  $\mu\text{m}$  were achieved at 8 V of input voltage. The large achievable deflections and the higher degree-of-freedom of the proposed device compared to its counterparts, foresee its use in diverse MEMS applications.

## 1 Introduction

Thermal actuation of microelectromechanical systems (MEMS) components is preferred to other types of actuation mechanisms such as electrostatic, piezoelectric, magnetic and pneumatic actuation for various reasons. Thermally actuated MEMS can achieve higher deflections

with considerable forces and can be operated at voltage levels that are compatible with today's IC and CMOS circuitries (<10 V). In addition, thermal microactuators demonstrate high repeatability and can be fabricated by IC-compatible manufacturing techniques (Comtois et al. 1995). Applications of microsystems that utilize thermal actuation include linear and rotary micromotors (Comtois et al. 1995), optical switches (Pai and Tien 1999), micro-mirrors (Cowan and Bright 1997), microgrippers (Chronis and Lee 2005) and variable capacitors (Yan et al. 2004).

Among the different types of thermal actuators, the horizontal U-shape microactuator is more common compared to the V-shape and bimorph actuation mechanisms. The horizontal U-shape microactuator has a narrow (hot) and wide (cold) arm. It operates based on the differential thermal expansion of these arms, when a voltage is applied between its two contact pads (Guckel et al. 1992). This basic microactuator has been improved in various ways to produce higher deflections. Notches were introduced on the arms to facilitate deflection (Lerch et al. 1996) and trenches were fabricated under the device to minimize heat loss to the substrate (Pan et al. 2005). Also, an additional hot arm was introduced so that the current could only travel along the hot arms, thus minimizing the power lost through the heating of the cold arm (Burns and Bright 1997). In addition to the wide variety of horizontally deflecting U-shape microactuators, vertically deflecting actuators have also been reported (Comtois and Bright 1997; Deladi et al. 2004; Yan et al. 2004; Atre 2006). However, all these microactuators exhibit only one degree-of-freedom (1-DOF), either horizontal or vertical, and they are restricted to move in only one direction, either positive or negative. This unidirectionality causes the microactuators to have a limited motion range. More recently, bidirectional electro-thermal actuators that can move either horizontally (Venditti et al.

---

C. Elbuken · N. Topaloglu · P. M. Nieva (✉) · M. Yavuz ·  
J. P. Huissoon  
Mechanical and Mechatronics Engineering,  
University of Waterloo, Waterloo, ON N2L 3G1, Canada  
e-mail: pniewa@uwaterloo.ca

2006) or vertically (Chen et al. 2003; Cao et al. 2007) have been proposed. However, these actuators are still limited to only 1-DOF. Larger deflection ranges and multidirectional actuation would tremendously enhance the motion range and applicability of electro-thermal actuators thus constituting a breakthrough in microactuation technology.

This paper presents a 2-DOF bidirectional actuator that operates purely with electro-thermal actuation. The microactuator is shown schematically in Fig. 1 and is composed of four narrow arms horizontally aligned, equally spaced, and connected to each other at one end. The outer arms are at a higher level compared to the inner arms. The connection at the ends of the top and the bottom arms is done by a large shuttle. Such a configuration is required to move the device independently in both actuation axes. By selectively applying voltage to two of its four pads, it can move bidirectionally (positive and negative) both in the horizontal and the vertical axis. By taking into account the thermal resistance of each arm, the horizontal and vertical motion is decoupled from each other, so the actuator can move independently in each axes. To the best of the authors' knowledge, there are only a few unidirectional 2-DOF actuators in the literature. Liao et al. (2002) and Wu and Hsu (2002) achieved 2-DOF motion by combining electro-thermal actuation with electrostatic and bimorph actuation, respectively. However, both of these designs have major drawbacks. First, the electrostatic actuation mechanism reported by Liao et al, requires very high voltages for the out-of-plane deflection (100 V for 3  $\mu\text{m}$  deflection). The design reported by Wu et al, requires large fixed-free structures making the release process difficult (Wu and Hsu 2002). Second, these microactuators could only deflect in one direction (either positive or negative) in two axes, therefore making them 2-DOF unidirectional actuators. Due to its multidirectional motion and ease of fabrication, the proposed electrothermal actuator foresees a large field of applications.

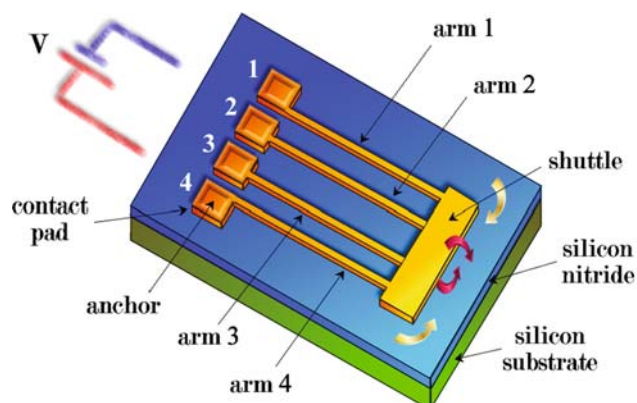


**Fig. 1** Schematic 3-D view of the 2-DOF bidirectional actuator (not to scale)

The paper is organized as follows. The different modes of operation are described first, followed by a lumped model that calculates the deflection in all directions as a function of the applied voltage. As an improvement to previous models found in the literature (Huang and Lee 1999; Yan et al. 2003), the lumped model presented here takes into account the heat loss due to conduction between all the arms of the electro-thermal actuator and the substrate, therefore yielding more accurate results. Finite element simulations of the device using ANSYS are then compared to the analytical model and the experimental results. Details of the fabrication using PolyMUMPs are also included.

## 2 Principle of operation

The operation of this 2-DOF bidirectional microactuator can be investigated using the four modes illustrated schematically in Fig. 2. Modes (a) and (b) represent the vertical deflection in the upward and downward direction, respectively; whereas modes (c) and (d) represent the horizontal deflections. The applied voltage configuration and the resultant direction of the displacement are also illustrated. During operation, depending on the desired direction of motion, two of the four arms are selectively heated. The two arms that are being actively heated are called the “active” arms. These arms are shown as thicker lines in Fig. 2. The remaining two arms are called the “passive”

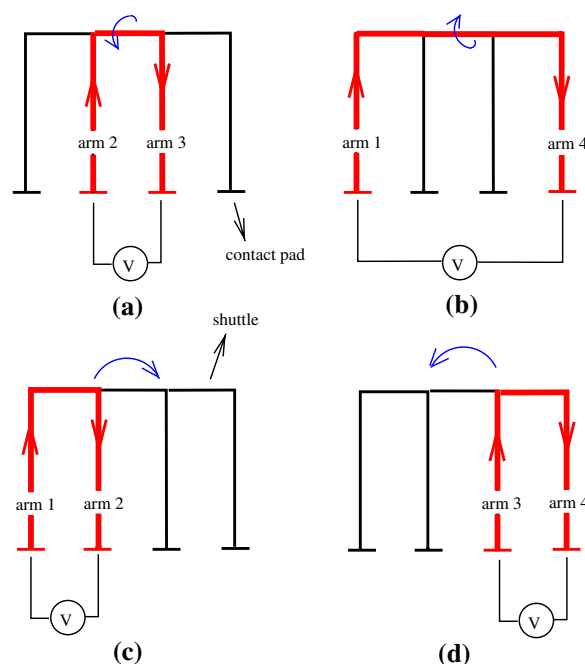


**Fig. 2** Operating modes of the 2-DOF bidirectional actuator. **a** Upward, **b** downward, **c** lateral to the right, and **d** lateral to the left modes

arms. The common “hot” and “cold” arm notation was not used, since this microactuator does not have a wide arm that is always kept colder compared to the narrow arm. As shown in Fig. 2a, b, for the upward (or downward) vertical deflection of the microactuator, voltage is applied to the inner (outer) arms. The increase in temperature due to the resistive heating causes these two arms to elongate. Since the arms are fixed from their connection points to the substrate, the heated arms deflect the tip of the device towards the other two arms. Deflection towards the passive arms results in the vertical motion of the tip due to the difference in the vertical position of these two sets of arms. Similarly, as also shown in Fig. 2c, d, for in-plane motion towards the left (right), voltage is applied to the rightmost (leftmost) two arms. The difference in the elongation of the active and passive arms results in the horizontal displacement of the tip.

The microactuator was designed to be consistent with the design rules of the Polysilicon Multi-user MEMS Process (PolyMUMPs) process offered by MEMSCAP (Carter et al. 2005). Fabrication details are included in Sect. 5. The basic microactuator design is shown schematically in Fig. 1. It should be noted that since the inner and outer arms were fabricated using Poly1 and Poly2, respectively, their resistivity and thickness are different. This difference results in different horizontal elongations during actuation. Consequently, for the two horizontal deflection modes (Fig. 2c, d), the active arms will expand different amounts yielding an additional undesired vertical deflection. Such a behavior was minimized by equating the thermal resistivities of the active arms and optimizing the arms length and/or width according to

$$R_T = \frac{1}{k_p} \frac{L}{wt}, \tag{1}$$

where  $k_p$  is the thermal conductivity and  $L$ ,  $w$  and  $t$  are the arm length, width and thickness, respectively. Using Eq. 1, the dimensions of the arms can be tailored to decouple the in-plane motion from the out-of-plane motion. On the other hand, for the two vertical deflection modes (Fig. 2a, b), the active arms are made of the same material and due to the symmetry of the design, undesired horizontal deflections are almost eliminated. The major asset of the proposed device is that independent in-plane and out-of-plane motion can be achieved by optimizing the dimensions of a single and simple structure.

### 3 Analytical model

The analysis of the 2-DOF bidirectional thermal actuator can be divided in two parts: electro-thermal analysis (Sect. 3.1) and thermo-mechanical analysis (Sect. 3.2).

#### 3.1 Electro-thermal analysis

The electro-thermal analysis is used to calculate the temperature distribution across all the arms of the 2-DOF microactuator. Figure 3 shows the schematic used to develop the electro-thermal model. For simplicity, the shuttle is assumed to have a constant cross-sectional area. The model determines the temperature distribution along the four arms ( $T_1$ ,  $T_2$ ,  $T_3$  and  $T_4$ ). Since the lengths of the arms ( $L_i$ ) are much larger than their thicknesses and widths, the heat can be assumed to flow in only one direction. Under this assumption, the heat distribution along the arms can be studied using a one-dimensional (1-D) heat transfer model.

As shown in Fig. 3, a potential difference  $V$  is applied between the pads of the arms 1 and 2. Using voltage division, the voltages across the active arms, 1 and 2, can be expressed as follows

$$V_1 = \frac{R_1}{R_1 + R_2 + R_{Lg1}} V \tag{2}$$

$$V_2 = \frac{R_2}{R_1 + R_2 + R_{Lg1}} V, \tag{3}$$

where  $R_1$ ,  $R_2$  and  $R_{Lg1}$  are the electrical resistances of the beams with lengths  $L_1$ ,  $L_2$  and  $L_{g1}$ , respectively.

The heat equation in each active arm can be derived by analyzing an infinitesimal portion of the arm. The analysis presented here is similar to the one used for a conventional three-arm electro-thermal microactuator by Yan et al. (2003). However, Yan et al. only considered the effect of the heat loss due to conduction between the hot arm and the substrate but not that of the cold arm. In fact, the discrepancies between the analytical and experimental results found in three-arm microactuators previously studied by other groups (Venditti et al. 2006; Yan et al. 2003) could be attributed to neglecting the cold arm heat losses, particularly at high operational voltages (7–10 V) (Yan et al. 2003). In our case, due to the narrow and similar widths of all the active and passive arms and the

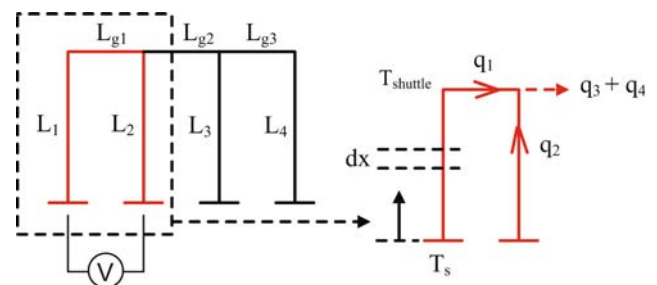


**Fig. 3** Schematic used for the development of the one-dimensional electro-thermal model of the 2-DOF electrothermal actuator

relatively small size of the shuttle, the analysis includes the heat loss due to heat conduction between all arms (including the shuttle) and the substrate. For simplicity, we have assumed that the heat is conducted only through the anchors and through the air-gap between the beam and the substrate. We have also assumed that the convective and radiative heat losses are negligible in comparison with the conductive losses (Fraser et al. 2006). Hence, if the substrate is considered a heat sink, the steady-state heat equation in an active beam  $i$  ( $i = 1, 2$ ) can be expressed as (Huang and Lee 1999)

$$k_p \frac{d^2 T_i(x)}{dx^2} = \frac{S_i(T_i(x) - T_s)}{R_{T,i} t_i} - \frac{V_i^2}{L_i^2 \rho}, \tag{4}$$

which can be re-written as

$$\frac{d^2 T_i(x)}{dx^2} = A_i(T_i(x) - T_s) - B_i, \tag{5}$$

where,

$$A_i^2 = \frac{S_i}{k_p R_{T,i} t_i} \quad \text{and} \quad B_i = \frac{V_i^2}{L_i^2 \rho k_p}. \tag{6}$$

In Eqs. 4–6,  $\rho$  is the electrical resistivity of polysilicon,  $t_i$  is the thickness of beam  $i$ ,  $T_i(x)$  is the temperature along the  $i$ th beam and  $T_s$  is the substrate temperature. The thermal resistance per unit area between the differential beam element and the substrate is denoted as  $R_{T,i}$  and can be expressed as the summation of the thermal resistance of the air gap and the nitride layer as

$$R_{T,i} = \frac{t_a}{k_a} + \frac{t_n}{k_n}, \tag{7}$$

where  $t_a$  and  $k_a$  are the thickness and the thermal conductivity of air, while  $t_n$  and  $k_n$  are the thickness and the thermal conductivity of the nitride layer, respectively. It should be noted that the air gap is smaller for the inner beams (arms 2 and 3), as they are built in Poly1. Since the substrate area is very large in comparison with the beam area, the heat flux lines spread apart as the heat is conducted away from the beam. To include this spreading effect in the model, the first term on the right hand side of Eq. 4 (i.e. the heat loss term) has been multiplied by a correction factor,  $S_i$ , given by Lin and Chiao (1996)

$$S_i = \frac{t_i}{w_i} \left( 2 \frac{t_a}{t_i} + 1 \right) + 1. \tag{8}$$

Equation 5 is valid for all active arms and its general solution is given by

$$T_1(x) = T_s + \frac{B_1}{A_1^2} + C_{11} e^{A_1 x} + C_{12} e^{-A_1 x} \tag{9}$$

$$T_2(x) = T_s + \frac{B_2}{A_2^2} + C_{21} e^{A_2 x} + C_{22} e^{-A_2 x}. \tag{10}$$

Since there is no heat generation along a passive arm, the heat Eq. 5 can be re-written as

$$k_p \frac{d^2 T_j(x)}{dx^2} = \frac{S_j(T_j(x) - T_s)}{R_{T,j} t_j} \tag{11}$$

or

$$\frac{d^2 T_j(x)}{dx^2} = A_j(T_j(x) - T_s), \tag{12}$$

where  $j = 3$  and  $j = 4$  correspond to arms 3 and 4 respectively, and  $A_j^2$ ,  $R_{T,j}$  and  $S_j$  can be calculated using Eqs. 6–8, respectively, by replacing  $i$  with  $j$ . The general solution of Eq. 12 for a passive arm can then be expressed as

$$T_3(x) = T_s + C_{31} e^{A_3 x} + C_{32} e^{-A_3 x} \tag{13}$$

$$T_4(x) = T_s + C_{41} e^{A_4 x} + C_{42} e^{-A_4 x}. \tag{14}$$

To determine the coefficients  $C_{mn}$  ( $m = 1, 2, 3, 4$ ;  $n = 1, 2$ ) in Eqs. 9, 10, 13 and 14, nine boundary conditions were used. The first eight boundary conditions correspond to the temperatures at the anchors and the tip of each beam and are given by,

$$T_m(0) = T_s \tag{15}$$

$$T_m(L_m) = T_{\text{shuttle}}, \tag{16}$$

where  $T_{\text{shuttle}}$  is the temperature of the shuttle which is assumed to be constant. The final boundary condition corresponds to the continuity of the heat flux at the tip (i.e. the shuttle). At this condition, the sum of the heat fluxes from the active arms should be equal to the outgoing heat towards the passive arms (Fig. 3).

$$q_1 + q_2 = q_3 + q_4, \tag{17}$$

where

$$q_1 = -k_p w_1 t_1 \left( \frac{dT_1}{dx} \right)_{x=L_1+L_{g1}} \tag{18}$$

$$q_2 = -k_p w_2 t_2 \left( \frac{dT_2}{dx} \right)_{x=L_2} \tag{19}$$

$$q_3 = \frac{(T_{\text{shuttle}} - T_s) k_p w_3 t_3}{L_3} \tag{20}$$

$$q_4 = \frac{(T_{\text{shuttle}} - T_s) k_p w_4 t_4}{L_4}. \tag{21}$$

The electro-thermal analysis described above is used to determine the temperature distribution across all the arms of the 2-DOF microactuator studied here. It should be

noted that this analysis can also be used with minor modifications to improve the analytical models for the previous three-arm microactuators. By accounting for the heat loss due to conduction between the cold arm and the substrate, the inaccuracy of the models at high operation voltages can be minimized.

### 3.2 Thermo-mechanical analysis

In this section, a thermo-mechanical analysis is coupled to the electro-thermal analysis to calculate the deflection at the tip of the microactuator due to the temperature distribution across the arms. For any given temperature distribution across the length of beam  $i$ , the thermal expansion can be found using the following expression

$$\Delta L_i = \alpha \int_0^{L_i} (T_i(x) - T_s) dx, \tag{22}$$

where  $\alpha$  is the coefficient of thermal expansion (CTE) of the beam material. The elongation of each beam can then be determined performing a structural analysis. The free-body diagram of the structure is shown schematically in Fig. 4.

The structural model of the four-arm actuator corresponds to a frame structure with four fixed supports. The structure is indeterminate with a degree of indeterminacy of nine. The deflection analysis has been made using the force method, which transforms the system into a statically determinate system and calculates the redundant forces required to keep the original geometry of the structure (Elms 1970). As shown in Fig. 4, three of the constraints are released and replaced by reaction forces and moments. The connection points of each one of the released arms will move in the longitudinal direction by  $\Delta L_1 - \Delta L_2$ ,  $\Delta L_1 - \Delta L_3$  and  $\Delta L_1 - \Delta L_4$ , respectively. To satisfy the restrictions at the supports, the connection points must be returned to their initial locations and orientations by applying the constraint forces  $X_i$ . The constraint forces are calculated from the following set of equations

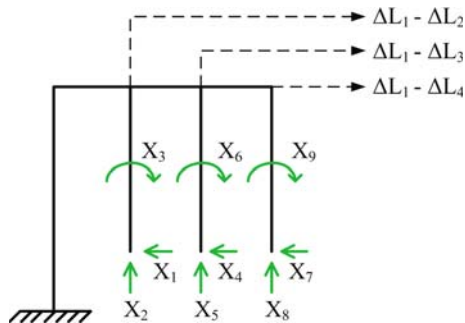


**Fig. 4** Free-body diagram of the microstructure showing the reaction forces and moments

$$\begin{bmatrix} f_{11} & \dots & f_{19} \\ \vdots & \ddots & \vdots \\ f_{91} & \dots & f_{99} \end{bmatrix} \begin{bmatrix} X_1 \\ X_2 \\ X_3 \\ X_4 \\ X_5 \\ X_6 \\ X_7 \\ X_8 \\ X_9 \end{bmatrix} = \begin{bmatrix} 0 \\ \Delta L_1 - \Delta L_2 \\ 0 \\ 0 \\ \Delta L_1 - \Delta L_3 \\ 0 \\ 0 \\ \Delta L_1 - \Delta L_4 \\ 0 \end{bmatrix}. \tag{23}$$

In Eq. 23, the  $9 \times 9$  matrix is known as the flexibility matrix. The flexibility matrix is composed of flexibility coefficients,  $f_{ij}$ s, which define the structure’s susceptibility to deform in the direction of  $X_i$  when  $X_j$  is applied. Once the reaction forces and moments are obtained, the deflection of the actuator tip can be calculated by the virtual work method. In this method, a virtual force  $P$  is applied to the tip of beam 1, as illustrated in Fig. 5. If the bending moment due to the virtual force is  $\bar{M}$  and the bending moment due to the reaction forces and moments is  $M$ , the total deflection at the actuator tip can be written as

$$u = \int_0^{L_1} \frac{\bar{M}M}{EI_1} dx, \tag{24}$$

where  $E$  and  $I_1$  are the Young’s modulus and the moment of inertia of beam 1, respectively. The moment diagrams for all beams are shown in Fig. 5.

The bending moment at position  $x$  due to the virtual force  $P$  can be written as

$$\bar{M} = (L_1 - x)P. \tag{25}$$

As can be seen in Fig. 5, the bending moment due to the reaction forces and moments,  $M$ , is the summation of three moments

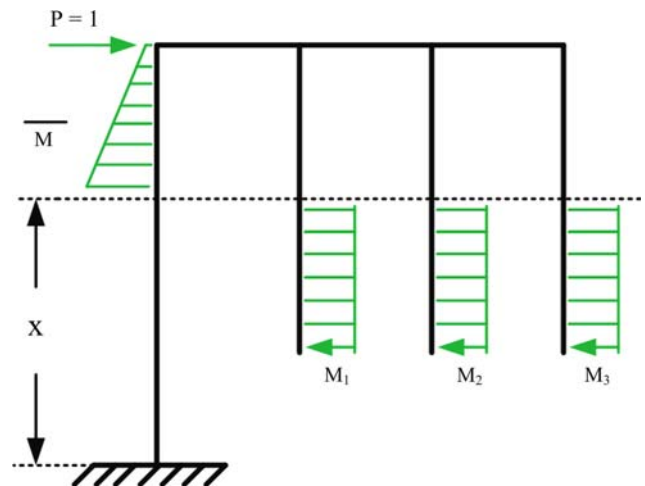


**Fig. 5** Moment diagram caused by the virtual force  $P$  and moments  $M_1$ ,  $M_2$  and  $M_3$

$$M = M_1 + M_2 + M_3. \tag{26}$$

Each bending moment can then be calculated as

$$M_1 = [x - (L_1 - L_2)]X_1 - X_2L_{g1} - X_3 \tag{27}$$

$$M_2 = [x - (L_1 - L_3)]X_4 - X_5(L_{g1} + L_{g2}) - X_6 \tag{28}$$

$$M_3 = [x - (L_1 - L_4)]X_7 - X_8(L_{g1} + L_{g2} + L_{g3}) - X_9, \tag{29}$$

where  $M_1$  is the bending moment due to  $X_1, X_2$  and  $X_3$ ;  $M_2$  is the bending moment due to  $X_4, X_5$  and  $X_6$  and  $M_3$  is the bending moment due to  $X_7, X_8$  and  $X_9$ . Substituting Eqs. 25–29 into Eq. 24, the horizontal deflection  $u$  can be found as

$$u = \frac{1}{EI_2} \left[ \frac{L^3}{6}(X_1 + X_4 + X_7) + \frac{L^2}{2}(H_1 + H_2 + H_3) \right], \tag{30}$$

where,

$$H_1 = X_1(L_2 - L_1) - X_2L_{g1} - X_3 \tag{31}$$

$$H_2 = X_4(L_3 - L_1) - X_5(L_{g1} + L_{g2}) - X_6 \tag{32}$$

$$H_3 = X_7(L_4 - L_1) - X_8(L_{g1} + L_{g2} + L_{g3}) - X_9. \tag{33}$$

The above analysis was performed to calculate the horizontal deflection of the arm. However, a similar procedure can be applied to find the vertical deflection. The similarity of the thermo-mechanical modeling for horizontal and vertical deflection is illustrated schematically in Fig. 6. Figure 6a, shows two arms in the horizontal deflection mode and Fig. 6b shows them in the vertical deflection mode. As it can be seen, the reaction forces are the same for the two modes except for the direction of  $X_1$  and  $X_3$ . The top view of the actuator frame in the horizontal deflection is the same as the side view of the vertical deflection. Hence, to calculate the deflection at the actuator tip in the vertical mode Eqs. 24–26 can be used. In this case,  $M_1, M_2$  and  $M_3$  are given by

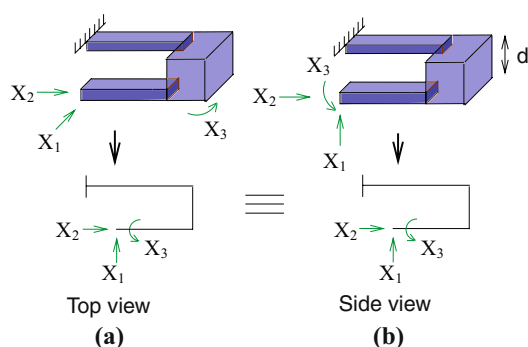


**Fig. 6** Schematic used for the thermo-mechanical modeling of the **a** horizontal and **b** vertical deflection of the arms of the 2-DOF microactuator

$$M_1 = [x - (L_1 - L_2)]X_1 - X_2d - X_3 \tag{34}$$

$$M_2 = [x - (L_1 - L_3)]X_4 - X_5d - X_6 \tag{35}$$

$$M_3 = [x - (L_1 - L_4)]X_7 - X_9, \tag{36}$$

where  $d$  is the vertical distance between the inner and the outer beams (refer to Fig. 6b). In addition, depending on the direction of deflection of the beams, a different flexibility matrix needs to be calculated. The rest of the procedure is analogous to the one described above for the horizontal deflection.

### 4 Simulations and results

A numerical simulation of a system such as the one described in here is especially important in order to take into account complex heat transfer mechanisms. In this work, simulations of the microactuator were performed using the finite element package ANSYS. The 3-D model of the system was developed using the structural coupled element solid98. For the simulations, we have considered the heat conduction between the active arms, passive arms and the substrate through the air gap and the heat convection from the side and top surfaces. Convective heat losses were introduced by setting up an air bounding box enclosing the actuator. The simulations were performed for various device dimensions. The geometric dimensions and the material constants used for the simulations were determined in accordance to the design specifications of PolyMUMPs. A complete list of simulation parameters are given in Table 1.

The temperature distribution for a bidirectional 2-DOF microactuator with 200  $\mu\text{m}$  long arms operated in the vertical mode (a) is shown in Fig. 7. For this mode, the input voltage is applied to the pads of the inner arms. The current is carried by a thin gold layer to the point where the arms are suspended. We have assumed that the temperature remains at 300 K at the contact pads and through the pad connections. As shown in Fig. 7, an input voltage of 5 V achieves a maximum temperature of 780 K along the active arms. The resultant tip deflection for the same applied voltage is shown in Fig. 8. As it can be seen, the elongation of the inner arms results in an upward tip movement of 3.98  $\mu\text{m}$ . A comparison of the 3-D simulation models of Figs. 7 and 8 shows that the actuator is tilted up.

The tip deflection has been plotted as a function of the input voltage in Fig. 9. Results are shown for both the analytical model (solid lines) and the ANSYS simulations (dashed lines) for each one of the four operational modes. It can be seen that the deflections increase non-linearly with increasing voltages for all the cases. The slight difference between the calculated and simulated values at

**Table 1** Material properties and geometrical parameters of the microactuator

Material properties (Carter et al. 2005)		Geometrical parameters	
Young's modulus of polySi	$162 \times 10^9$ Pa	Length of arm 1, arm 4	200 $\mu\text{m}$
Poisson's ratio	0.22	Length of arm 2, arm 3	200 $\mu\text{m}$
Thermal conductivity of polySi	$41 \times 10^{-6}$ W $\mu\text{m}^{-1}$ C $^{-1}$	Width of arm 1, arm 4	4 $\mu\text{m}$
Thermal conductivity of nitride	$2.25 \times 10^{-6}$ W $\mu\text{m}^{-1}$ C $^{-1}$	Width of arm 2, arm 3	2.5 $\mu\text{m}$
Thermal conductivity of air	$0.026 \times 10^{-6}$ W $\mu\text{m}^{-1}$ C $^{-1}$	Thickness of arm 1, arm 4	1.5 $\mu\text{m}$
Thermal expansion coefficient	$3.5 \times 10^{-6}$ C $^{-1}$	Thickness of arm 2, arm 3	2 $\mu\text{m}$
Convection coefficient	$10 \times 10^{-12}$ W $\mu\text{m}^{-2}$ C $^{-1}$	Device-substrate distance	2 $\mu\text{m}$
Resistivity of Poly1	20 $\Omega\mu\text{m}$	Gap between adjacent arms	4 $\mu\text{m}$
Resistivity of Poly2	30 $\Omega\mu\text{m}$	Width of the shuttle	12 $\mu\text{m}$

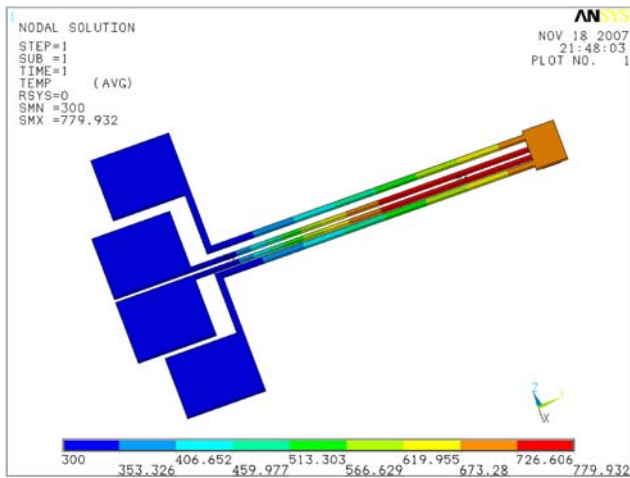


**Fig. 7** Results of the ANSYS finite element simulations showing the temperature distribution of a 200  $\mu\text{m}$  long microactuator operating in the vertical mode (a)

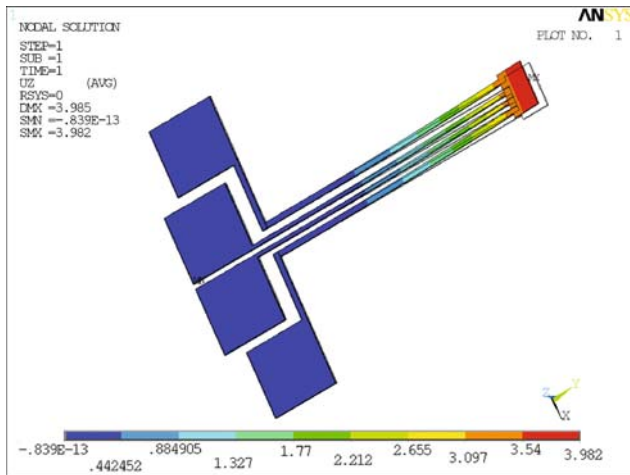


**Fig. 8** Results of the ANSYS finite element simulations showing the deflection of a 200  $\mu\text{m}$  long microactuator operating in the vertical mode (a)

higher voltages could be attributed to the size of the air bounding box enclosing the device during the ANSYS simulations which was limited by the number of elements

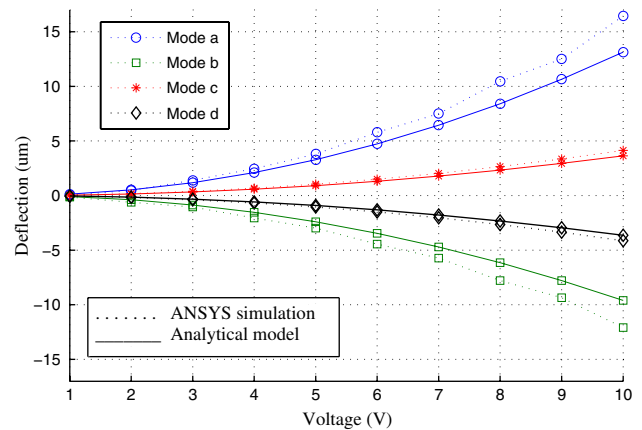


**Fig. 9** Comparison of the analytical model and the ANSYS simulations 200  $\mu\text{m}$  long operating between 1 and 10 V

required for the meshing. Due to this fact, the convective heat loss in the simulations might have been underestimated resulting in higher temperatures and hence higher deflections.

The 2-DOF bidirectional microactuator deflects the same in the two horizontal actuation modes (c) and (d). However, there is a difference of about 30% between the two deflection modes along the vertical axis [(a) and (b)]. In fact, Fig. 9 shows that the out-of-plane displacement of the device is always larger than the in-plane displacement for the same input voltage. We believe that this is due to the different structural and material properties of the inner and outer arms and the higher vertical compliance of the structure that stems from the fact that the thickness of the arms are smaller than their widths. It can also be observed that upward vertical deflections are greater than downward vertical deflections for the same input voltage. This behavior can be attributed to the difference in the thermal resistance of the inner and outer arms. When thermal resistances are not equal, the arm with higher resistance heats up to higher temperatures and elongates more, causing greater deflections in the corresponding mode. For example, according to the analytical model, at 8 V of

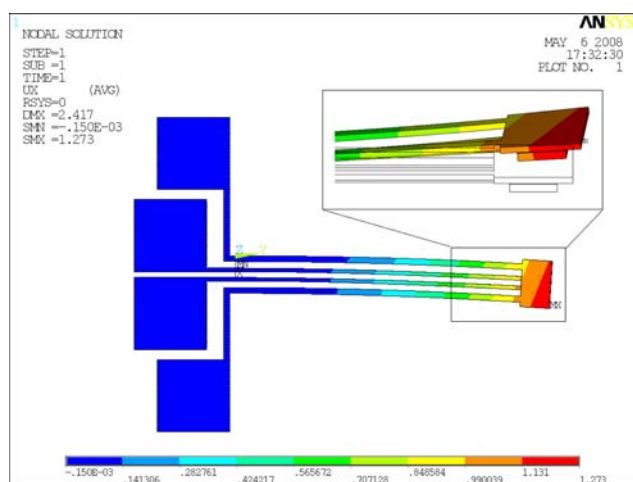


**Fig. 10** Diagonal motion of a 200  $\mu\text{m}$  long 2-DOF bidirectional microactuator. ANSYS simulation results show a 1.27  $\mu\text{m}$  in-plane deflection and a 2  $\mu\text{m}$  out-of-plane deflection simultaneously

potential difference, the tip deflection is 8.4, 6.1, 2.3 and 2.3  $\mu\text{m}$  in modes (a), (b), (c) and (d), respectively. Therefore, the motion range of the microactuator at 8 V is 14.5 and 4.6  $\mu\text{m}$  for out-of-plane and in-plane deflections, respectively. Notice that due to the bidirectional motion, the deflections in both directions on each axis have been added up to calculate the total motion range.

Although the study of the diagonal motion of this microactuator is not within the scope of this paper, it should be noted here that diagonal deflections can also be achieved by simultaneously applying voltage to three of the four contact pads. For example, Fig. 10 shows the resulting diagonal motion of the 200  $\mu\text{m}$  long microactuator using ANSYS simulations. In this simulation, 6 V and 2 V were applied to pad-2 and pad-3, respectively while grounding pad-1. As seen in Fig. 10, simulation results show a simultaneous in-plane deflection of 1.27  $\mu\text{m}$  and out-of-plane deflection of 2  $\mu\text{m}$ .

## 5 Fabrication and characterization

The 2-DOF bidirectional microactuator was fabricated using PolyMUMPs run 78. A scanning electron micrograph of the microactuator is shown in Fig. 11. PolyMUMPs is a three-layer polysilicon MEMS surface micromachining process (Carter et al. 2005) that uses a 600 nm LPCVD (low pressure chemical vapor deposition) silicon nitride film as isolation. The 2.0  $\mu\text{m}$  thick first polysilicon structural layer (Poly1) was used to form the inner arms (2 and 3). The 2.0  $\mu\text{m}$  thick PSG (phosphosilicate glass) sacrificial layer was patterned and etched to form their anchors. The second 0.75  $\mu\text{m}$  thick PSG sacrificial layer forms the vertical air-gap between the inner and outer arms. This layer

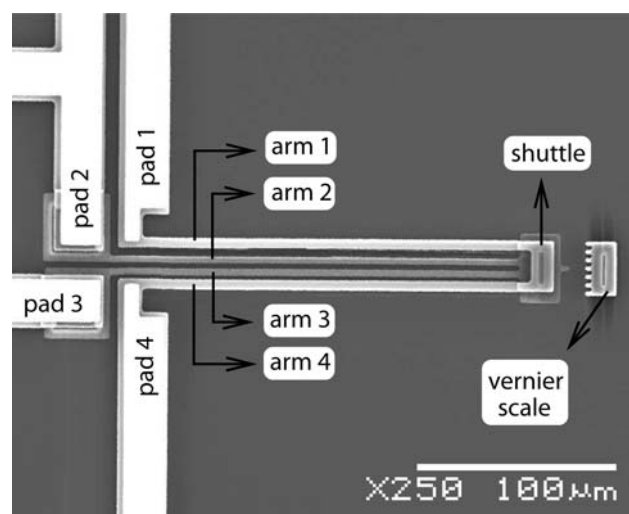


**Fig. 11** Scanning electron micrograph (SEM) of a 200  $\mu\text{m}$  long 2-DOF bidirectional microactuator fabricated using PolyMUMPs Run 78

was patterned using the via mask to form the connection between the inner and the outer arms to the shuttle. The outer arms (1 and 4) are made in the PolyMUMPs second structural layer (Poly2), which is 1.5  $\mu\text{m}$  thick. The 0.5  $\mu\text{m}$  thick gold layer is used to form the contact pads (100  $\mu\text{m}$   $\times$  100  $\mu\text{m}$ ). Vernier scales were included at the tip of the actuators to facilitate the measurements. The microactuators were released by immersing the chips in a 49% HF solution followed by CO<sub>2</sub> critical point drying to avoid stiction. As previously stated, a list of the material properties and the geometric parameters of the device studied in this paper have been included in Table 1.

The in-plane deflection tests were performed under an optical microscope with a CCD camera. The voltage was applied to the devices using DC microprobes. For the characterization of actuation mode (c), the probes were placed on contact pads 1 and 2 (refer to Fig. 11). Similarly, contact pads 3 and 4 were used for actuation mode (d). The potential difference between the contact pads was varied between 1 and 10 V and the motion of the actuator was recorded using optical micrographs taken at 1 V increments. Figure 12 shows an optical micrograph of the tip motion in actuation mode (d) obtained using an input voltage of 6 V. The tip deflection was measured using the vernier scale and for this particular case, was found to be 1.5  $\mu\text{m}$ .

The out-of-plane deflections were measured using laser interferometry. A 5 mW He-Ne (Helium-Neon) laser beam, with a wavelength of  $\lambda = 633$  nm, was shined on the microactuator to create interference patterns. For example, when a potential difference is applied between the two Poly1 arms, the actuator tilts up and the air-gap distance between the arms and the substrate varies along the arms forming interference patterns that can be easily

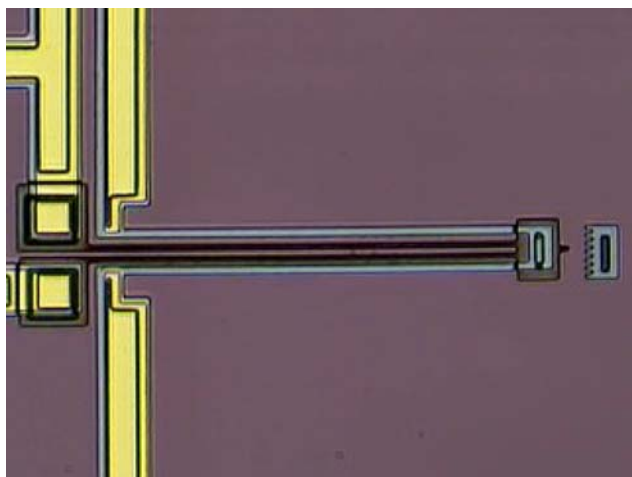


**Fig. 12** Optical image of a 200 μm long 2-DOF bidirectional microactuator operated in mode (d) using 6 V of input voltage

observed and recorded using a CCD camera. Optical images showing the interference patterns for three vertical deflection measurements are shown in Fig. 13 at different input voltages (1, 4 and 7 V). In these pictures, a pair of bright and dark fringes corresponds to a height difference

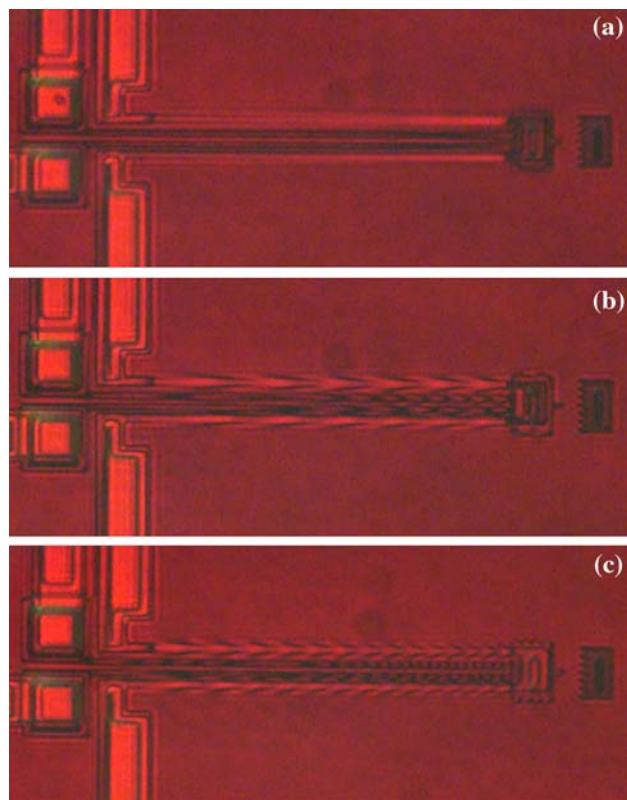


**Fig. 13** Optical images of a 200 μm long 2-DOF bidirectional microactuator operated in mode (a) showing interference patterns observed using a 5 mW He–Ne laser beam ( $\lambda = 633$  nm) at different input voltages, **a** 1 V; **b** 4 V and **c** 7 V

of  $\lambda/2$  which is around  $0.317 \mu\text{m}$ . Thus, by counting the number of bright and dark fringes along one of the arms of the actuator, one can determine the amount of total vertical deflection. It can be observed that the number of fringes and thus the deflection increases exponentially with increasing voltage. A Matlab program was developed to count the fringes and determine the total deflection of the microactuators. In this program, the intensities of the red color components of the pixels along the beam were plotted. Each local maximum and local minimum denoted a bright and a dark fringe, respectively. The vertical tip displacement was calculated by multiplying the total number of maxima by  $0.317$ .

The experimental results for in-plane [modes (c) and (d)] and out-of-plane [mode (a)] deflections are compared to the deflections calculated using the analytical model in Fig. 14 for a voltage range between 1 and 10 V. As can be observed from this figure, within this voltage range, the tested displacement values closely match the values calculated analytically. For example, at 8 V, the deflection was measured as 8.2, 2.5 and  $2.4 \mu\text{m}$  in modes (a), (c) and (d), respectively. In general, the experimental results verify that the 2-DOF bidirectional microactuator can easily achieve decoupled in-plane and out-of-plane deflections up to voltages around 10 V. However, voltages above 10 V caused excessive heating of the arms which was observed by the change in color along the arms. In addition, the maximum in-plane and out-of-plane deflections before failure due to melting of polysilicon were measured as  $9 \mu\text{m}$  (at 14 V and 102 mW) and  $23 \mu\text{m}$  (at 15 V and 154.5 mW), respectively. Furthermore, the downward deflection could not be completely verified due to the

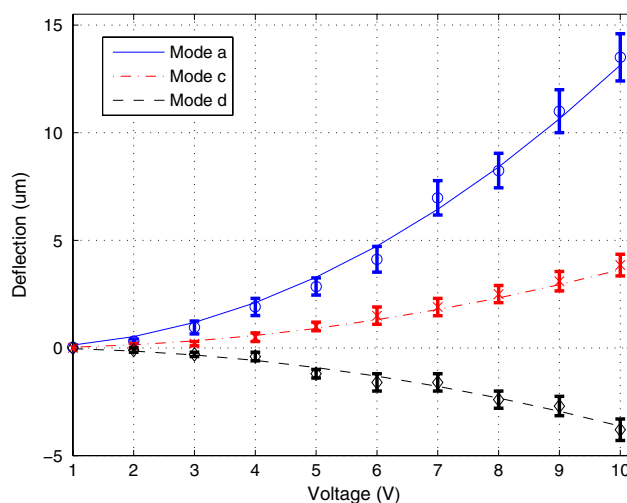


**Fig. 14** Achievable deflections versus input voltage for a 2-DOF bidirectional microactuator with 200 μm long beams. The experimental results are shown with error margins and are compared to the analytical results

presence of the substrate underneath the actuator and limitations imposed by the interferometric test method. However, the ANSYS simulation results presented in Sect. 4 predicts a downward deflection of approximately  $8\ \mu\text{m}$  using an input voltage of  $8\ \text{V}$  (refer to Fig. 9).

The operation range of the 2-DOF bidirectional micro-actuator presented here is constrained by the design requirements of PolyMUMPs. However, its performance can be improved by customizing the fabrication process. For instance, the substrate under the actuator can be cut to make the device usable in all four operation modes. Using the same input voltages, larger horizontal displacement values can be obtained by overlapping the inner and outer arms or by using narrower arms. Similarly, the vertical displacements can be increased by decreasing the thickness of the arms.

## 6 Conclusion

In this study, a 2-DOF bidirectional microactuator was introduced. Electro-thermal actuation was employed to achieve the multidirectional motion. Decoupled vertical and horizontal operational modes of the device were demonstrated. A two-step analytical model was developed to calculate the tip deflection as a function of the input voltage. The analysis provided in this paper could be used with minor modifications to improve previous models used for the study of conventional three-arm electro-thermal microactuators (Venditti et al. 2006; Yan et al. 2003). Finite element based simulations using ANSYS were performed to validate the analytical models. The experimental results obtained for the microactuators fabricated using PolyMUMPs match the analytical and simulation results very closely up to  $10\ \text{V}$ . Based on these results, total in-plane deflections of  $4.8\ \mu\text{m}$  ( $2.4\ \mu\text{m}$  in either direction) were achieved using for example  $8\ \text{V}$  of input voltage. During out-of-plane operation, the tip deflection in the upward direction can reach up to  $8.2\ \mu\text{m}$  at the same input voltage. The fact that this 2-DOF bidirectional actuator can be easily fabricated using PolyMUMPs and can move independently in two axes makes it ideal for various MEMS applications.

## References

- Atre A (2006) Analysis of out-of-plane thermal microactuators. *J Micromech Microeng* 16(2):205–213
- Burns DM, Bright VM (1997) Design and performance of a double hot arm polysilicon thermal actuator. In: *Proc SPIE int soc opt eng*. Austin, TX, USA, pp 296–306
- Cao A, Kim J, Lin L (2007) Bi-directional electrothermal electro-magnetic actuators. *J Micromech Microeng* 17(5):975–982
- Carter J, Cowen A, Hardy B, Mahadevan R, Stonefield M, Wilcenski S (2005) POLYMUMPs design handbook revision v11.0. <http://www.memscap.com/mumps/documents>, mEMSCAP Inc.
- Chen WC, Chu CC, Hsieh J, Fang W (2003) A reliable single-layer out-of-plane micromachined thermal actuator. *Sens Actuators A Phys* A103:48–58
- Chronis L, Lee LP (2005) Electrothermally activated SU-8 microgripper for single cell manipulation in solution. *J Microelectromech Syst* 14(14):857–863
- Comtois JH, Bright VM (1997) Applications for surface-micromachined polysilicon thermal actuators and arrays. *Sens Actuators A Phys* A58:19–25
- Comtois CH, Bright VM, Phipps MW (1995) Thermal microactuators for surface-micromachining processes. In: *Proc SPIE int soc opt eng*. Austin, TX, USA, pp 10–21
- Cowan WD, Bright VM (1997) Vertical thermal actuators for micro-opto-electro-mechanical systems. In: *Proc SPIE int soc opt eng*. Austin, TX, USA, pp 127–146
- Deladi S, Krijnen G, Elwenspoek MC (2004) Parallel-beams/lever electrothermal out-of-plane actuator. *Microsyst Technol* 10:393–399
- Elms DG (1970) *Linear elastic analysis*. B. T. Batsford Ltd, London
- Fraser J, Hubbard T, Kujath M (2006) Theoretical and experimental analysis of an off-chip microgripper. *Can J Electr Comput Eng* 31:77–81
- Guckel H, Klein J, Christenson T, Skrobis K, Laudon M, Lovell EG (1992) Thermo-magnetic metal flexure actuators. In: *IEEE solid-state sensor and actuator workshop*, New York, NY, USA, pp 73–75
- Huang QA, Lee NKS (1999) Analysis and design of polysilicon thermal flexure actuator. *J Micromech Microeng* 9(1):64–70
- Lerch P, Slimane CK, Romanowicz B, Renaud P (1996) Modelization and characterization of asymmetrical thermal micro-actuators. *J Micromech Microeng* 6(1):134–137
- Liao KM, Chueh CC, Chen R (2002) A novel electro-thermally driven bi-directional microactuator. In: *Proc 2002 intal symp on micromechatronics and human science*, Nagoya, Japan, pp 267–274
- Lin L, Chiao M (1996) Electrothermal responses of lineshape microstructures. *Sens Actuators A Phys* A55:35–41
- Pai M, Tien NC (1999) Operating principles of an electrothermal vibrometer for optical switching applications. In: *Proc SPIE int soc opt eng*, Santa Clara, CA, USA, pp 124–130
- Pan CH, Chang CL, Chen YK (2005) Design and fabrication of an electro-thermal microactuator with multidirectional in-plane motion. *J Microlithogr Microfabr Microsyst* 4:1–15
- Venditti R, Lee JSH, Sun Y, Li D (2006) An in-plane, bi-directional electrothermal MEMS actuator. *J Micromech Microeng* 16(10):2067–2070
- Wu CT, Hsu W (2002) An electro-thermally driven microactuator with two dimensional motion. *Microsyst Technol* 8:47–50
- Yan D, Khajepour A, Mansour R (2003) Modeling of two-hot-arm horizontal thermal actuator. *J Micromech Microeng* 13(2):312–322
- Yan D, Khajepour A, Mansour R (2004) Design and modeling of a MEMS bidirectional vertical thermal actuator. *J Micromech Microeng* 14(7):841–850